5-3-2024

Biallelic BORCS8 variants cause an infantile-onset neurodegenerative disorder with altered lysosome dynamics.

Raffaella De Pace

Reza Maroofian

Adeline Paimboeuf

Mina Zamani

Maha S. Zaki

See next page for additional authors

Recommended Citation

De Pace R, Maroofian R, Paimboeuf A, et al. Biallelic BORCS8 variants cause an infantile-onset neurodegenerative disorder with altered lysosome dynamics. Brain. 2024;147(5):1751-1767. doi:10.1093/brain/awad427

BRAIN
ORIGINAL ARTICLE

Biallelic *BORCS8* variants cause an infantile-onset neurodegenerative disorder with altered lysosome dynamics

Raffaella De Pace,[1,†] Reza Maroofian,[2,†] Adeline Paimboeuf,[3,†] Mina Zamani,[4,5] Maha S. Zaki,[6] Saeid Sadeghian,[7] Reza Azizimalamiri,[7] Hamid Galehdari,[4] Jawaher Zeighami,[5] Chad D. Williamson,[1] Emily Fleming,[8] Dihong Zhou,[8,9] Jennifer L. Gannon,[9,10] Isabelle Thiffault,[8,11] Emmanuel Roze,[12] Mohnish Suri,[13] Giovanni Zifarelli,[14] Peter Bauer,[14] Henry Houlden,[2] Mariasavina Severino,[15] Shunmoogum A. Patten,[3,16] Emily Farrow[9,17] and Juan S. Bonifacino[1]

[†]These authors contributed equally to this work.

BLOC-one-related complex (BORC) is a multiprotein complex composed of eight subunits named BORCS1–8. BORC associates with the cytosolic face of lysosomes, where it sequentially recruits the small GTPase ARL8 and kinesin-1 and -3 microtubule motors to promote anterograde transport of lysosomes toward the peripheral cytoplasm in non-neuronal cells and the distal axon in neurons. The physiological and pathological importance of BORC in humans, however, remains to be determined. Here, we report the identification of compound heterozygous variants [missense c.85T>C (p.Ser29Pro) and frameshift c.71-75dupTGGCC (p.Asn26Trpfs*51)] and homozygous variants [missense c.196A>C (p.Thr66Pro) and c.124T>C (p.Ser42Pro)] in *BORCS8* in five children with a severe early-infantile neurodegenerative disorder from three unrelated families.

The children exhibit global developmental delay, severe-to-profound intellectual disability, hypotonia, limb spasticity, muscle wasting, dysmorphic facies, optic atrophy, leuko-axonopathy with hypomyelination, and neurodegenerative features with prevalent supratentorial involvement.

Cellular studies using a heterologous transfection system show that the BORCS8 missense variants p.Ser29Pro, p.Ser42Pro and p.Thr66Pro are expressed at normal levels but exhibit reduced assembly with other BORC subunits and reduced ability to drive lysosome distribution toward the cell periphery. The BORCS8 frameshift variant p.Asn26Trpfs*51, on the other hand, is expressed at lower levels and is completely incapable of assembling with other BORC subunits and promoting lysosome distribution toward the cell periphery.

Therefore, all the *BORCS8* variants are partial or total loss-of-function alleles and are thus likely pathogenic. Knockout of the orthologous *borcs8* in zebrafish causes decreased brain and eye size, neuromuscular anomalies and impaired locomotion, recapitulating some of the key traits of the human disease.

These findings thus identify *BORCS8* as a novel genetic locus for an early-infantile neurodegenerative disorder and highlight the critical importance of BORC and lysosome dynamics for the development and function of the central nervous system.

1 Neurosciences and Cellular and Structural Biology Division, Eunice Kennedy Shriver National Institute of Child, Health and Human Development, National Institutes of Health, Bethesda, MD 20892, USA
2 Department of Neuromuscular Disorders, UCL Queen Square Institute of Neurology, London WC1N 3BG, UK
3 Institut National de la Recherche Scientifique (INRS), Centre Armand Frappier Santé Biotechnologie, Laval, QC H7V 1B7, Canada

Received April 11, 2023. Revised September 30, 2023. Accepted December 02, 2023. Advance access publication December 21, 2023
Published by Oxford University Press on behalf of the Guarantors of Brain 2023.

4 Department of Biology, Faculty of Science, Shahid Chamran University of Ahvaz, Ahvaz 83151-61355, Iran
5 Department of Molecular Genetics, Narges Medical Genetics and Prenatal Diagnosis Laboratory, Ahvaz 61556-89467, Iran
6 Human Genetics and Genome Research Institute, Clinical Genetics Department, National Research Centre, Cairo 12622, Egypt
7 Department of Pediatric Neurology, Golestan Medical, Educational, and Research Center, Ahvaz Jundishapur University of Medical Sciences, Ahvaz 61357-33184, Iran
8 Department of Genetics, Children's Mercy Kansas City, Kansas City, MO 64108, USA
9 Department of Pediatrics, University of Missouri-Kansas City School of Medicine, Kansas City, MO 64108, USA
10 Division of Clinical Genetics, Children's Mercy Kansas City, Kansas City, MO 64108, USA
11 Department of Pathology, Children's Mercy Kansas City, Kansas City, MO 64108, USA
12 Sorbonne Université, CNRS, INSERM, Institut du Cerveau (ICM), and Assistance Publique-Hôpitaux de Paris, Department of Neurology, Hôpital de la Pitié-Salpêtrière, Paris 75013, France
13 Nottingham Clinical Genetics Service, Nottingham University Hospitals NHS Trust, City Hospital Campus, Nottingham NG5 1PB, UK
14 CENTOGENE GmbH, 18055 Rostock, Germany
15 Neuroradiology Unit, IRCCS Istituto Giannina Gaslini, Genoa 16147, Italy
16 Départementde Neurosciences, Université de Montréal, Montréal, QC H3C 3J7, Canada
17 Genomic Medicine Center, Children's Mercy Kansas City, Kansas City, MO 64108, USA

Correspondence to: Dr Juan S. Bonifacino
Neurosciences and Cellular and Structural Biology Division
Eunice Kennedy Shriver National Institute of
Child Health and Human Development (NICHD)
National Institutes of Health (NIH), Building 35
Room 2F-226, 35A Convent Drive, MSC 3758
Bethesda, MD 20892-3758, USA
E-mail: juan.bonifacino@nih.gov

Correspondence may also be addressed to: Dr Emily Farrow
Department of Genetics, Children's Mercy Hospital
2401 Gilham Road, 3rd Floor East CMRI
3902.15, Kansas City, MO 64108, USA
E-mail: egfarrow@cmh.edu

Dr Shunmoogum (Kessen) A. Patten
INRS—Centre Armand Frappier Santé Biotechnologie
531 Boul. des Prairies, Laval, QC H7V 1B7, Canada
E-mail: kessen.patten@inrs.ca

Keywords: lysosomes; neurodevelopmental disorder; neurodegeneration; leukodystrophy; hereditary spastic paraplegia

Introduction

BLOC-one-related complex (BORC) is a ubiquitously expressed protein complex composed of eight subunits named BORCS1–8.[1] BORC associates with the cytosolic face of lysosomal and late endosomal organelles (herein collectively referred to as 'lysosomes') at least in part through a myristoyl group at the N-terminus of BORCS5[1] and an interaction of BORCS6 with the ragulator complex.[1-4] BORC then promotes the recruitment of the small GTPase ARL8 (which in mammals exists as two paralogues, ARL8A and ARL8B)[5] to lysosomes.[1] In turn, ARL8 recruits the motor proteins kinesin-1 (via the adaptor protein PLEKHM2/SKIP)[6] and kinesin-3 (directly).[7] BORC/ARL8-mediated coupling to these kinesins enables anterograde transport of lysosomes along microtubule tracks toward the peripheral cytoplasm in non-polarized cells[1,6,8] and the distal axon in neurons.[9-11] The ability of lysosomes to move within the cytoplasm is critical for many cellular functions, including cell adhesion and migration,[1,12] invasive cancer growth,[13] plasma membrane repair,[14] metabolic signalling[15,16] and maintenance of axonal health.[9,11]

Homozygous ablation of the *Borcs5*[9] or *Borcs7*[11] genes in mice (*Borcs5*$^{-/-}$ or *Borcs7*$^{-/-}$ mice, respectively) causes neonatal lethality due to suffocation and/or failure to feed in the first hours of life. Homozygous mice bearing a spontaneous truncating mutation (p.Q87X) in Borcs7 (*Borcs7*$^{Q87X/Q87X}$) are viable, but develop progressive axonal dystrophy and impairment of motor function.[11] Analyses of cortical and hippocampal neurons cultured from *Borcs5*$^{-/-}$, *Borcs7*$^{-/-}$ or *Borcs7*$^{Q87X/Q87X}$ embryonic day (E)15–18 embryos revealed clustering of lysosomes in the soma and their depletion from the axon.[9,11] Moreover, immunohistochemical analyses of tissues from *Borcs5*$^{-/-}$ mice showed reduced staining for lysosomes in axon-enriched regions of the corpus callosum and molecular layer of the hippocampus, and at neuromuscular junctions (NMJs) in the diaphragm.[9] Finally, axons in the phrenic and spinal nerves were found to contain numerous eosinophilic dystrophic bodies or spheroids indicative of degeneration.[9]

These studies thus revealed that, despite the ubiquitous presence of BORC in many cells and tissues, the pathologic consequences of its deficiency are mainly manifested in the CNS.

To date, little is known about the importance of BORC in human physiology and pathology. A study involving whole-exome sequencing in 31 mostly consanguineous Arab families with neurologic disease identified a c.203-1G>T biallelic splice variant in *BORCS5* (referred to as *LOH12CR1* in that study) in a patient featuring autosomal recessive developmental delay, microcephaly, seizures, cortical malformation, polymicrogyria and agenesis of the corpus callosum.[17] However, this study did not provide a detailed clinical characterization of the patient nor a functional analysis of the variant protein.

Here, we report five children from three independent families presenting with a severe neurodegenerative disorder associated with biallelic variants in *BORCS8*. The children exhibit global developmental delay, intellectual disability, hypotonia, spasticity, muscle wasting, dysmorphic facies, optic atrophy, leuko-axonopathy with hypomyelination, and neurodegenerative features with prevalent supratentorial involvement. Cellular studies using a heterologous transfection system show that the variant proteins exhibit reduced assembly with other BORC subunits and reduced ability to promote lysosome distribution toward the cell periphery. Moreover, *borcs8*-KO zebrafish display neurodevelopmental defects, recapitulating some of the key traits of the human disease. These studies thus identify *BORCS8* as a novel gene locus for an early-infantile neurodegenerative disorder and demonstrate the critical importance of BORC for the development and function of the CNS.

Material and methods

Patient ascertainment and clinical and molecular studies

Three unrelated families of European-American (Family FI), Iranian-Arab (Family FII) and Egyptian ancestry (Family FIII) were recruited and studied (Fig. 1A and Supplementary Fig. 1). The study was approved by the institutional ethics committees of the Children's Mercy Kansas City Hospital (Children's Mercy IRB# 11120514) and University College London (IRB# 310045/1571740/37/598), and written informed consent was obtained from all three families in accordance with the Declaration of Helsinki. De-identified skin fibroblasts from the patients and the mother of the European-American family were shared with the National Institutes of Health (NIH) laboratory for research purposes. Skin fibroblasts from a healthy individual (Individual 85E0344) and from an SPG50 patient that carries pathogenic mutations in the *AP4M1* and *ATS* genes (Patient 87RD39)[18,19] were used as controls. Detailed clinical features, photos, videos, brain MRI, family history and clinical notes were obtained from all affected individuals and reviewed by a group of clinical geneticists, dysmorphologists and paediatric neurologists. Brain MRIs were reviewed by an experienced paediatric neuroradiologist. Genome, exome and Sanger sequencing were performed independently at three different research and clinical laboratories, as previously described.[20-22]

Culture and transfection of human cells lines

HEK293T cells, HeLa cells and human skin fibroblasts were cultured in Dulbecco's modified Eagle medium (DMEM) (Quality Biological), supplemented with 2 mM L-glutamine (GIBCO), 10% fetal bovine serum (FBS, GIBCO), 100 U/ml penicillin-streptomycin (GIBCO) (complete DMEM) in a 37°C incubator (5% CO_2, 95% air). HeLa cells grown on six-well plates were transiently transfected with 0.8 μg plasmid DNA using 2 μl Lipofectamine 2000 (Invitrogen), according to the manufacturer's instructions. Approximately 24 h after transfection, cells were replated onto 12-mm coverslips coated with collagen. Cells were then cultured for an additional 24 h before fixation and immunofluorescent labelling. This longer transfection period was necessary for rescue of the BORC phenotype. For the co-immunoprecipitation and MG132 treatment experiments, HEK293T cells grown on 10 cm plates were transiently transfected for 48 h with 8 μg plasmid DNA and 25 μl Lipofectamine 2000 (Invitrogen) according to the manufacturer's instructions. One plate was used for the transfection of each construct in each experiment.

HeLa BORCS8 knockout generation and genotyping

BORCS8-KO HeLa cells were generated using CRISPR-Cas9, as described.[23] Briefly, the *BORCS8*-targeting guide RNAs TTTCCC GGTTCGCTCGGCCG and CTTTAATTACCGGTCCCCCC were cloned separately into pSpCas9 (BB)-2A-GFP plasmid (Addgene, 48138; from Feng Zhang). HeLa cells were co-transfected with the two plasmids and, after 48 h, GFP-positive cells were selected on a FACSAria II cell sorter (BD Biosciences). Single-cell clones were isolated on 96-well plates. After 21 days, genomic DNA was extracted and the region around the targeted sequences amplified by PCR with TTGTCCGCAAAGACTGAGGAG and AGCGATTACTACGCCC CG primers. Genotyping of wild-type (WT) and BORCS8-KO HeLa cells generated 745-bp and 513-bp fragments, respectively. The resulting deletion of part of the first exon and first intron in *BORCS8* was confirmed by Sanger sequencing of the amplified region.

SDS-PAGE and immunoblotting

Cells were washed twice with ice-cold PBS (Corning), scraped from the plates in 1× Laemmli sample buffer (1× LSB) (Bio-Rad) supplemented with 2.5% v/v 2-mercaptoethanol (Sigma-Aldrich), heated at 95°C for 5 min, and resolved by SDS-PAGE. Gels were blotted onto nitrocellulose membrane and blocked with 5% w/v non-fat milk in Tris-buffered saline, 0.1% v/v Tween 20 (TBS-T) for 20 min. Membranes were sequentially incubated with primary antibody and secondary HRP-conjugated antibody diluted in TBS-T. SuperSignal West Dura Reagents (Thermo Fisher) were used for detection of the antibody signal with a Bio-Rad Chemidoc MP imaging system. Controls for sample loading were either GAPDH or β-actin.

Immunoprecipitation

Transfected HEK293T cells were lifted in ice-cold PBS and centrifuged at 500*g* for 5 min. The pellet was washed twice with ice-cold PBS and lysed in 10 mM Tris-Cl pH 7.5, 150 mM NaCl, 0.5 mM EDTA, 0.5% v/v Nonidet P40 supplemented with a protease inhibitor cocktail (Roche). Cell lysates were clarified by centrifugation at 17 000*g* for 10 min and the supernatant (10% was saved as input) was incubated with anti-HA magnetic agarose beads (Thermo Fisher) at 4°C for 1 h. After three washes with 10 mM Tris-Cl pH 7.5, 150 mM NaCl, 0.5 mM EDTA, the precipitates were eluted with 1× LSB at 95°C for 5 min. The immunoprecipitated samples and inputs were analysed by SDS-PAGE and immunoblotting.

Immunofluorescence microscopy

Cells were seeded on collagen-coated coverslips in 24-well plates at 40 000 cells per well in regular culture medium. Cells were then

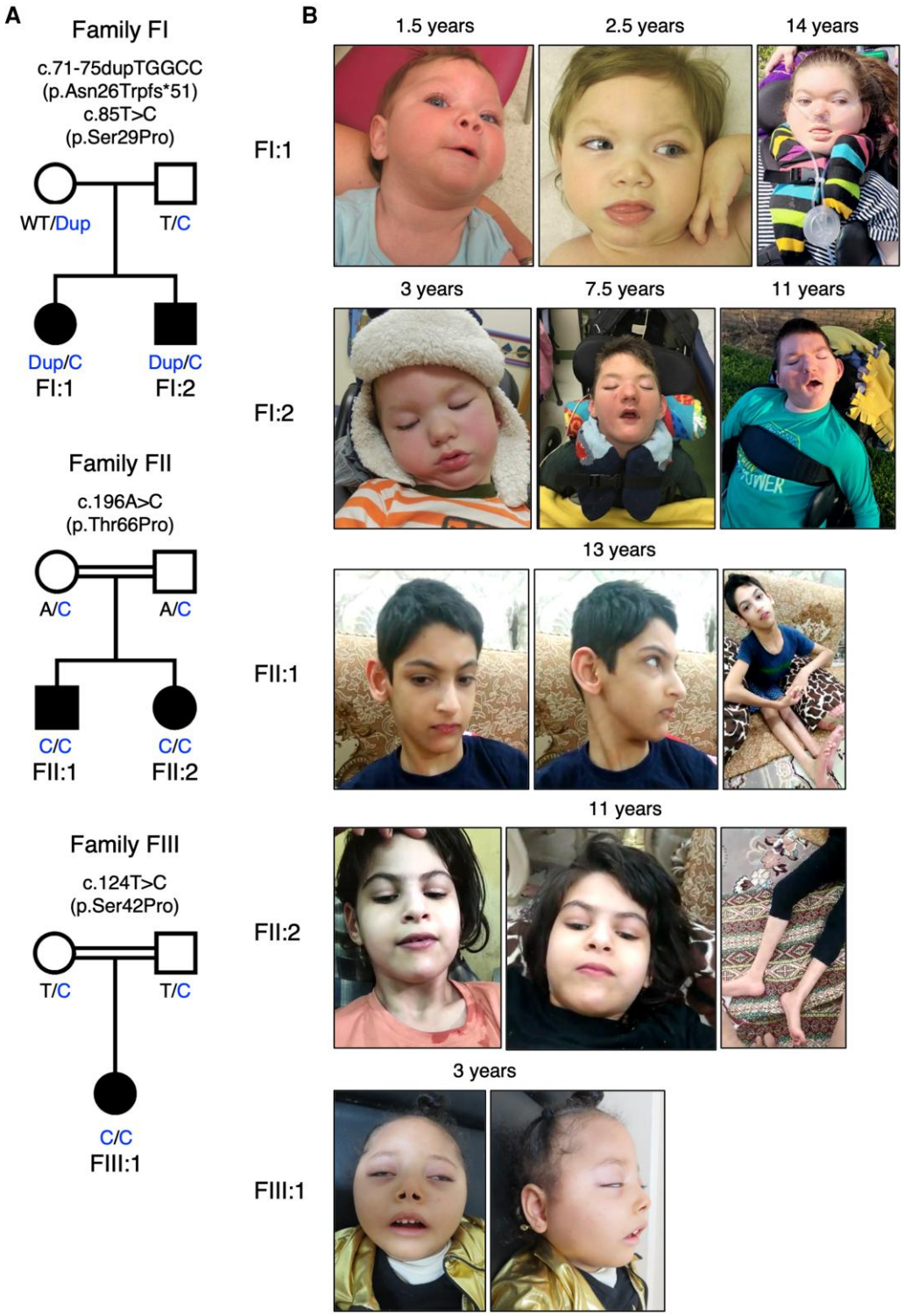

Figure 1 Family pedigrees and photographs of the patients. (**A**) Family pedigrees and genotypes. *BORCS8* variants are indicated, with Dup corresponding to the c.71-75dupTGGCC (p.Asn26Trpfs*51) variant, and T/C and A/C to the T>C and A>C single-base substitution variants, respectively. (**B**) Photographs of the patients at the indicated ages.

fixed in 4% w/v paraformaldehyde (Electron Microscopy Sciences) in PBS for 20 min, permeabilized and blocked with 0.1% w/v saponin, 1% w/v bovine serum albumin (BSA, Gold Bio) in PBS for 20 min, and sequentially incubated with primary and secondary antibodies diluted in 0.1% w/v saponin, 1% w/v BSA in PBS for 30 min at 37°C. Coverslips were washed three times in PBS and mounted on glass slides using Fluoromount-G (Electron Microscopy Sciences) with DAPI. Z-stack cell images were acquired on a Zeiss LSM 780 inverted confocal microscope (Carl Zeiss) using a Plan-Apochromat 63× objective (NA = 1.4). Maximum intensity projections were generated with Zeiss ZEN Black software and final composite images were created using ImageJ/Fiji (https://fiji.sc/).

Zebrafish methods

Wild-type *Danio rerio* (AB/TL strain) were maintained at 28°C at a light/dark cycle of 12/12 h in accordance with standard practices.[24] Embryos were raised at 28.5°C and collected and staged, as previously described.[25] All experiments were performed in compliance with the guidelines of the Canadian Council for Animal Care and the local ethics committee of INRS. For immunohistochemical studies, pigment formation was blocked by adding 0.003% phenylthiourea (PTU) dissolved in egg water at 24 h after fertilization (hpf).

Additional materials and methods

Additional materials and methods are described in the Supplementary material. These include materials and methods for work with human cells (culture of human skin fibroblasts, prediction of BORC complex structure, plasmids, antibodies and chemicals) and zebrafish [generation of *borcs8* F0 KO zebrafish and rescue experiments, behavioural assays, phalloidin staining, analysis of NMJ morphology, motor axon visualization, haematoxylin and eosin brain staining and acetylcholinesterase (AChE) activity].

Statistical analyses

Band intensities of BORC subunits in immunoblots from three to four independent experiments were determined using Image Lab (Bio-Rad) and normalized to β-actin or GAPDH. To quantify the distribution of LAMP1, cells were plated on collagen, imaged and maximum intensity projections of *z*-stack confocal micrographs were subjected to shell analysis.[26] Briefly, cells exhibiting morphologies where perinuclear clusters of lysosomes were situated too close to the plasma membrane were excluded from analysis. Cell outlines were traced in Fiji (https://imagej.net/software/fiji/) and the total fluorescence of LAMP1 signal was measured. Using the 'enlarge' function in Fiji, the cell outline was shrunk by 2 μm and LAMP1 signal intensity remeasured. The intensity of LAMP1 signal within the peripheral 2-μm shell was plotted as percentage of total cellular LAMP1 signal. One-way ANOVA, followed by multiple comparisons using the Dunnett's or Tukey's test, was used for statistical analysis of most datasets; the paired Student's *t*-test was used when comparing two datasets. All zebrafish experiments were performed on at least three replicates (*N*), and each consisted of a sample size (*n*) of 8–72 fish. All zebrafish data values are given as means ± standard error of the mean (SEM). Significance for the zebrafish experiments was determined using either Student's *t*-test or one-way ANOVA followed by multiple comparisons test. Statistical analyses were done using Prism version 9 (GraphPad Software).

Results

Clinical findings

This study involved three unrelated families (Families FI, FII and FIII) with five children (Patients FI:1, FI:2, FII:1, FII:2 and FIII:1) presenting with an early-infantile neurological disorder (Fig. 1A and Supplementary Fig. 1). Clinical and genetic analyses were conducted as described below and summarized in Table 1 and

Table 1 Summary of genotypes and phenotypes of the *BORCS8* variant patients

Patients	Patient FI:1	Patient FI:2	Patient FII:1	Patient FII:2	Patient FIII:1
Zygosity	Compound heterozygous	Compound heterozygous	Homozygous	Homozygous	Homozygous
Coding sequence changes	85T>C, 71-75dupTGGCC	85T>C, 71-75dupTGGCC	196A>C	196A>C	124T>C
Amino acid changes	Ser29Pro, Asn26Trpfs*51	Ser29Pro, Asn26Trpfs*51	Thr66Pro	Thr66Pro	Ser42Pro
Gender	Female	Male	Male	Female	Female
Ethnicity	European-American	European-American	Arab-Iranian	Arab-Iranian	Egyptian
Consanguinity	No	No	Yes	Yes	Yes
Age at last follow-up	14 years	11 years	13 years	11 years	3 years
Hypotonia	Yes	Yes	Yes	Yes	Yes
Failure to thrive	Yes	Yes	Yes	Yes	Yes
Global developmental delay	Yes	Yes	Yes	Yes	Yes
Intellectual disability	Profound	Profound	Profound	Profound	Profound
Microcephaly	No	No	Yes	Yes	Yes
Muscle weakness and atrophy	Yes	Yes	Yes	Yes	Yes
Seizures	Yes	Yes	No	No	Yes
Spasticity	Yes	Yes	Yes	Yes	No
Scoliosis	Yes	Yes	Yes	No	No
Dysmorphic features	Yes	Yes	Yes	Yes	Yes
Optic atrophy	Yes	Yes	Not assessed	Yes	Yes
Other clinical features	Restrictive lung disease, chronic respiratory disease, osteoporosis, G-tube dependency, impaired oropharyngeal motility, oral and pharyngeal dysphagia, hearing loss, urosepsis, chronic UTI	Chronic respiratory insufficiency, restrictive lung disease, chronic ear infections, osteoporosis, G-tube dependency, sensitive, dry skin	No	No	Recurrent chest infections due to aspiration, recurrent choking, feeding difficulties, bowel and urinary incontinence, sparse hair

For additional details, see Supplementary Table 1. UTI = urinary tract infection.

Supplementary Tables 1 and 2. Dysmorphology analyses are summarized in Supplementary Table 3.

Patient FI:1

Patient FI:1 (Fig. 1A and B and Supplementary Fig. 1) is a 14-year-old European-American female, the first child born to non-consanguineous parents. She was delivered after induction at 39 weeks of gestation due to maternal hypertension. The fetal movements were described as normal, with normal ultrasound exams. At birth, she weighed 3.23 kg and her length was 52.07 cm. She was discharged home after 24 h. She had normal development until 3–4 months of age, with no subsequent developmental progress, including walking and speech acquisition. At ~1 year of age, she was noted to smile and laugh, but it was unclear if the laughter was an appropriate response. She developed seizures at 15 months of age, including generalized tonic seizures and recurrent myoclonic seizures. At 10 years of age, she weighed 36.1 kg with an occipitofrontal circumference (OFC) of 53 cm. She had a dry scalp and face, hypertelorism, arched thick eyebrows, up-slanting palpebral fissures, bulbous nasal tip, anteverted nares, protruding tongue that peels, dry full lips (Fig. 1B and Supplementary Table 3), scoliosis, abnormal postures of the four limbs predominating in the distal parts, muscle atrophy in legs and arms, global hypotonia with absent patellar reflexes, and a history of bilateral femur fractures, kidney stones, cortical visual impairment with optic atrophy, airway clearance issues and G-tube dependency. At 14 years of age, she is non-verbal, wheelchair-dependent and needs support for head control and sitting independently (Fig. 1B and Supplementary Video 1). Previous negative clinical testing includes chromosomal microarray, karyotype, analysis of mitochondrial tRNA, leukodystrophy panel, hereditary spastic paraplegia panel and symptom-driven exome.

Brain MRI at 1 year of age showed moderate cerebral white matter volume reduction and delayed myelination associated with ventricular dilatation, thin corpus callosum, mild enlargement of the cerebral subarachnoid spaces and very small thalami (Supplementary Fig. 2A–D). The pons and inferior cerebellar vermis were small with associated mega cisterna magna, while the cerebellar hemispheres volume and cerebellar white matter signal were normal (Supplementary Fig. 2A–D). A follow-up MRI at 9 years of age showed disease progression with severe cerebral atrophy, enlargement of the subarachnoid spaces and lack of myelination progression, additional focal T_2/FLAIR signal alterations in the frontal periventricular regions, further reduction of the thalamic volume and optic nerve atrophy (Fig. 2). Marked T_2 hypointensity and T_1 hyperintensity of the globi pallidi were also noted (Supplementary Fig. 3A–D).

Patient FI:2

Patient FI:2 (Fig. 1A and B and Supplementary Fig. 1) is an 11-year-old European-American male, the second child born to the same parents as Patient FI:1. He was born at 37 weeks of gestation following a pregnancy complicated by maternal hypertension and gestational diabetes, which was monitored. Prenatal ultrasounds were normal. At delivery, he weighed 3.2 kg and was 48.3-cm long. The umbilical cord was reported to be wrapped around his neck and he required oxygen for 15 min; however, he was discharged home after 3–4 days with no further complications. He had normal development until 3–4 months of age, with no subsequent developmental progress, including walking and speech acquisition. He developed intractable seizures by 1 year of age. At 7 years of age, he weighed 27.2 kg with an OFC of 52.5 cm. A physical exam found dry skin on scalp and face, hypotonic facies, hypertelorism, arched thick eyebrows, up-slanting palpebral fissures, very large ears, bulbous nasal tip, anteverted nares, high palate, thick full lips (Fig. 1B and Supplementary Table 3), bilateral everted ankles, contractures in knees and some finger joints, muscle atrophy in arms and legs, global hypotonia and absent patellar reflexes. Additionally, he had airway clearance issues and G-tube dependency. At 11 years of age, he remains non-verbal, wheelchair-dependent, and needs support for head control and sitting independently (Fig. 1B and Supplementary Video 2). Other genetic testing included chromosomal microarray, karyotype and an epilepsy sequencing panel, which showed normal or non-diagnostic results.

Brain MRI performed at 7.7 years of age revealed moderate volume reduction and lack of myelination of the supratentorial white matter with consequent ventricular enlargement and thin corpus callosum (Fig. 2). Additional focal T_2 signal alterations were noted in the frontal and parietal periventricular regions. Moderate-to-severe cerebral cortical atrophy with enlargement of the subarachnoid spaces was present. The thalami and pons were small. The cerebellar white matter signal was normal while the foliar CSF spaces were slightly enlarged (Fig. 2). Finally, a right optic nerve glioma and left optic nerve atrophy were noted (Supplementary Fig. 3E–G). He had a resection of the optic nerve glioma at 7.5 years of age.

Patient FII:1

Patient FII:1 (Fig. 1A and B and Supplementary Fig. 1) is a 13-year-old male, the first child of a consanguineous Iranian-Arab family. The healthy parents are first cousins. The patient's prenatal and perinatal history were unremarkable and he was born at term with his growth parameters all within normal range (2.75 kg weight, 59 cm length). However, his development was significantly delayed in all domains. At present, he is non-verbal and has no eye contact with others, and his level of cognitive impairment is in the range of severe-to-profound (Supplementary Video 3). Medical examination at the age of 13 years showed postnatal microcephaly, failure to thrive, no language and hand skills, inability to walk, head nodding stereotypies, hand rubbing/wringing stereotypies, drooling, tongue thrusting, axial hypotonia, muscle atrophy and lower limb spasticity (Fig. 1B and Supplementary Video 3). He had a Babinski sign and brisk tendon reflexes (Supplementary Video 3). His vision was poor, but hearing was within normal range. Facial dysmorphism included long and narrow face, upswept anterior hairline, prominent supraorbital ridges, deep-set eyes, thick arched eyebrows, long eyelashes, long or large ears, high nasal bridge, full nasal tip, low-set columella, bow-shaped upper lip, flared alae nasi and tall chin (Fig. 1B, Supplementary Table 3 and Supplementary Video 3). Additionally, he had long and slender fingers, broad and round distal thumbs, long toes, over-riding of hallux and third toe by second toe, deep plantar crease, thin trunk and extremities (Fig. 1B, Supplementary Table 3 and Supplementary Video 3).

Brain MRI at 1 year of age demonstrated moderate white matter volume reduction and delayed myelination with associated ventricular dilatation, especially in the parieto-occipital regions, thin corpus callosum, mild enlargement of the cerebral subarachnoid spaces and very small thalami (Supplementary Fig. 2E–H). The pons and inferior cerebellar vermis were small with associated mega cisterna magna, while the cerebellar hemispheres volume and cerebellar white matter signal were normal (Supplementary Fig. 2E–H). Follow-up MRI at 13 years of age showed disease progression with moderate cerebral and cerebellar atrophy, lack of myelination progression, further reduction of the thalamic volume, mild

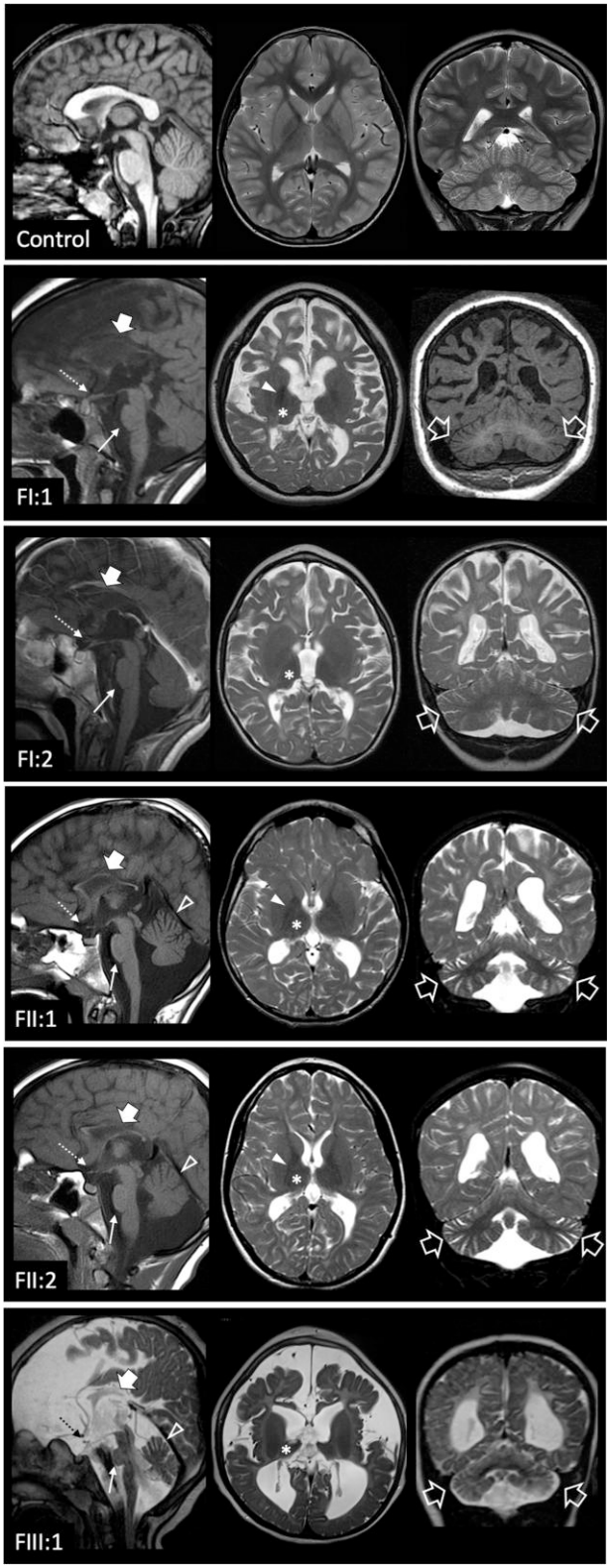

Figure 2 Neuroimaging findings. Brain MRI studies of a control subject performed at 9 years of age for comparison, and of the patients performed at 9 years (Patient FI:1), 7.7 years (Patient FI:2), 13 years Patient FII:1), 12 years (Patient FII:2) and 3 years of age (Patient FIII:1). In the patients, sagittal T_1- or T_2-weighted (*left*), axial T_2-weighted (*middle*) and coronal T_1 or T_2-weighted images (*right*) reveal mild-to-severe cerebral atrophy with reduced white matter volume and enlarged subarachnoid spaces in all cases. There is diffuse T_2 hyperintensity of the cerebral

(Continued)

T_2 hypointensity of the globi pallidi and optic nerve atrophy (Fig. 2). Additional focal T_2/FLAIR signal alterations were noted in the frontal and parietal periventricular regions, with an 'ears of the lynx' pattern in the frontal lobes (Supplementary Fig. 3H and I).

Patient FII:2

Patient FII.2 (Fig. 1A and B and Supplementary Fig. 1) is an 11-year-old female, the second child of the Iranian-Arab Family FII. Her prenatal and perinatal history and metabolic investigations were unremarkable. She was born at term with normal growth parameters (3 kg weight, 48 cm length). However, she had global developmental delay with severe-to-profound intellectual disability and failure to thrive. At present, she cannot speak and has no eye contact with others. Neurological examination at 11 years of age showed postnatal microcephaly, no language, no hand skills, inability to walk, hand rubbing/wringing stereotypies, axial hypotonia, and spasticity and muscle atrophy of the lower limbs (Supplementary Video 4). She has a Babinski sign and brisk tendon reflexes (Supplementary Video 4). Ophthalmic examination at the age of 2 years revealed bilateral optic atrophy. Hearing was normal. She has facial dysmorphic features including bifrontal narrowing, arched eyebrows, synophrys, full nasal tip and prominent heels (Fig. 1B, Supplementary Table 3 and Supplementary Video 4).

Brain MRI performed at 2 years of age revealed mild volume reduction and diffuse T_2 hyperintensity of the cerebral white matter in keeping with absent myelination, with associated ventricular dilatation especially in the parieto-occipital regions, thin corpus callosum, mild enlargement of the cerebral subarachnoid spaces and very small thalami (Supplemental Fig. 2I–L). Additional focal T_2/FLAIR signal alterations were noted in the frontal and parietal periventricular regions, with an anterior 'ears of the lynx' pattern lobes (Supplementary Fig. 3J and K). The cerebellar volume and white matter signal were normal (Supplementary Fig. 2I–L). Follow-up brain MRI at 12 years of age showed disease progression with mild cerebral and moderate cerebellar atrophy, lack of myelination progression, further reduction of the thalamic volume, mild T_2 hypointensity of the globi pallidi and optic nerves atrophy (Fig. 2). The fronto-parietal periventricular T_2/FLAIR signal alterations were accentuated (Fig. 2).

Patient FIII:1

Patient FIII.1 (Fig. 1A and B and Supplementary Fig. 1) is a 3-year-old female, the only child of a consanguineous Egyptian family. Parents are healthy and there is no history of similar conditions reported in the extended family. The pregnancy history noted weak fetal movement and maternal pre-eclampsia and delivery was by elective Caesarean section. The measurements at birth were: 3.1 kg weight, 48 cm length and 33.5 cm OFC. After birth, she was irritable, had excessive crying and refused to suckle. At the end of the first day, she was admitted to the NICU for 8 days, where

Figure 2 Continued
white matter in all subjects, with relative sparing of the internal capsules and subcortical U-fibres in Patients FII:1 and FII:2, in keeping with hypomyelination. Focal signal alterations are associated at the level of the fronto-parietal white matter. The corpus callosum is thin in all patients (thick arrows). The thalami are very small and slightly T_2 hypointense in all cases (asterisks). The globi pallidi are small and darker on T_2-weighted images in Patients FI:1, FII:1 and FII:2 (full arrowheads). There is mild pontine hypoplasia (thin arrows) and marked optic nerve and chiasm atrophy (thin dashed arrows) in all subjects. Mild-to-moderate cerebellar atrophy with prevalent enlargement of the hemispheric subarachnoid spaces is present in all subjects (empty arrows), while involvement of the superior vermis is visible only in Patients FII:1, FII:2 and FIII:1 (empty arrowheads).

hyperbilirubinaemia and hypocalcaemia were recorded. Her developmental milestones were severely delayed. She did not acquire any motor or cognitive skills and had an apparently progressive course as she had some visual tracking and social smile at 3 months old. She suffered from recurrent choking spells followed by chest infections. On examination, she was lethargic, encephalopathic, not reacting to her surroundings and had absent speech. Seizures started at the age of 8 months, were intractable with myoclonic and focal patterns, recurred four to eight times per day, did not respond to several drug combinations including valproate, levetiracetam, vigabatrin, topiramate and clonazepam. The anthropometric measurements at 3 years of age identified a weight of 13 kg, length of 85 cm and OFC of 45 cm. The patient had a hypotonic face, a sloping forehead, sparse hair, wide-spaced eyes, an upturned nose, long philtrum, retruded mandible and low-set ears (Fig. 1B and Supplementary Table 3). General examination was unremarkable and neurological evaluation showed generalized hypotonia (both axial and limbs) with hyporeflexia. Laboratory tests showed normal karyotype, metabolic screening, acylcarnitine profile, organic acid in urine, ammonia and lactate in plasma, and auditory brainstem response (ABR). Liver transaminases were elevated (ALT: 113 and AST: 52). EEG revealed subcortical epileptogenic discharges. Pallor of the optic nerves was observed at fundus oculi examination. Brain MRI performed at 3 years of age showed severe cerebral and mild cerebellar atrophy with supratentorial ventricle dilatation, lack of supratentorial white matter myelination with sparing of the cerebellar white matter, thin corpus callosum, very small thalami, optic nerve atrophy, and pontine and inferior vermis hypoplasia with mega cisterna magna (Fig. 2).

Identification of biallelic variants in *BORCS8*

In Family FI, quad familial research exome and genome sequencing of DNA from the affected siblings (Patients FI:1 and FI:2) and their parents identified two variants in *trans* in *BORCS8*: a maternally inherited frameshift variant [NM_001145783.2:c.71_75dup(p.Asn26Trpfs*51)] and a paternally inherited missense variant [NM_001145783.2:c.85T>C(p.Ser29Pro)] (Fig. 1A). The frameshift variant is not present in ~2 000 000 alleles/chromosomes across multiple large, aggregated sequence databases (Supplementary Table 2). This variant results in substitution of Trp for Asn-26 and replacement of the remaining 93 amino acids by 49 extraneous amino acids (henceforth denoted N26W*) (Fig. 3A and B). The missense variant, on the other hand, is present in 35 carriers in the European population. This variant encodes a substitution of Pro for the highly conserved Ser-29 [Genomic Evolutionary Rate Profiling (GERP) score 4.71 and Combined Annotation Dependent Depletion (CADD) score 25.6] (Fig. 3A and B and Supplementary Table 2) and is predicted to be damaging/deleterious and disease-causing by most *in silico* tools (Supplementary Table 2).

In Family FII, research exome sequencing of DNA from the two siblings (Patiens FII:1 and FII:2), confirmed by Sanger sequencing, identified a novel homozygous *BORCS8* missense variant [(NM_001145784.2):c.196A>C (p.Thr66Pro)] (Fig. 1A). This variant is within a sizable region of homozygosity and is absent from all the inspected variant databases. It encodes a substitution of Pro for the highly conserved Thr-66 (GERP score 4.24 and CADD score 28.4) (Fig. 3A and B and Supplementary Table 2) and is predicted to be damaging/deleterious and disease-causing by most *in silico* tools (Supplementary Table 2).

In Family FIII, clinical exome sequencing of the proband (Patient FIII-1) identified a novel homozygous missense variant in *BORCS8* [(NM_001145784.2):c.124T>C (p.Ser42Pro)] residing within a large region of homozygosity. This variant was not observed in any variant frequency databases. It encodes a substitution of Pro for the highly conserved Ser-42 (GERP score 4.71 and CADD score 28.3) (Fig. 3A and B) and is predicted to be damaging/deleterious and disease-causing by the majority of employed *in silico* tools (Supplementary Table 2).

In all three families, no additional variants of unknown significance, pathogenic or likely pathogenic, associated with neurodevelopmental or neurodegenerative disorders were identified.

BORCS8 encodes a protein of 119 amino acids named BORCS8 or MEF2BNB (https://www.ncbi.nlm.nih.gov/gene/729991). BORCS8 is a subunit of the hetero-octameric BORC (Fig. 3C–E), previously shown to mediate ARL8-dependent regulation of lysosome motility and positioning.[1] The N26W* variant removes most of a predicted long α-helix (Fig. 3C–E), resulting in a protein with only 25 N-terminal amino acids from the normal protein, followed by an irrelevant sequence. The substitutions to Pro in the missense variants likely cause destabilization by disruption of the long α-helix.

Reduced assembly of BORCS8 variants

To determine the properties of the patients' variants in cells, we obtained cultured skin fibroblast from Patients FI:1 and FI:2, and from their unaffected mother as a control. Cells from Families FII and FIII were not available for analysis. Immunoblot and immunofluorescence microscopy analyses for BORCS8 itself in Family FI fibroblasts were unsuccessful because several commercial and house-made antibodies failed to recognize the endogenous protein. As an alternative, we performed immunoblot analysis of the fibroblasts for BORCS5 and BORCS7, for which there are suitable antibodies. For this analysis, we also included two additional human skin fibroblast cultures from a healthy individual (Control 1: 85E0344) and from an SPG50 patient that carries pathogenic mutations in the *AP4M1* and *ATS* genes (Control 2: 87RD39).[18,19] This analysis revealed no significant differences in the levels of BORCS5 and BORCS7 in fibroblasts from the mother and the unrelated controls, but a significant 45%–60% reduction in BORCS5 and BORCS7 levels in the patient's fibroblasts relative to fibroblasts from the mother and the unrelated controls (Fig. 3F and G). These findings indicated that the *BORCS8* N26W* and S29P variants resulted in reduced levels of other BORC subunits. Quantitative real-time reverse-transcription PCR (qRT-PCR) revealed equal levels of *BORCS8*, *BORCS5* and *BORCS7* mRNAs in fibroblasts from the mother and both patients (Supplementary Fig. 4A and B), indicating that the variants did not decrease mRNA levels but likely destabilized the corresponding proteins.

To directly analyse the effect of the individual variants on the expression and assembly of BORCS8 itself, we next used a heterologous system in which wild-type and BORCS8-mutant proteins tagged with a C-terminal HA epitope were expressed by transient transfection in HEK293T cells. Immunoblotting of cell extracts showed that whereas the wild-type, S29P, T66P and S42P mutants were expressed at similar levels, the N26W* mutant was expressed at ~40% levels of the wild-type and other mutants (Fig. 4A–D, 10% input lanes). Real-time qRT-PCR showed that the wild-type, N26W* and S29P *BORCS8* mRNAs were expressed at similar levels (Supplementary Fig. 4C). Incubation with the proteasome inhibitor MG132 did not change the levels of wild-type and S29P but increased the levels of N26W* BORCS8 (Fig. 4E). These findings are consistent with the lower levels of the N26W* mutant protein being at least partly due to proteasomal degradation.

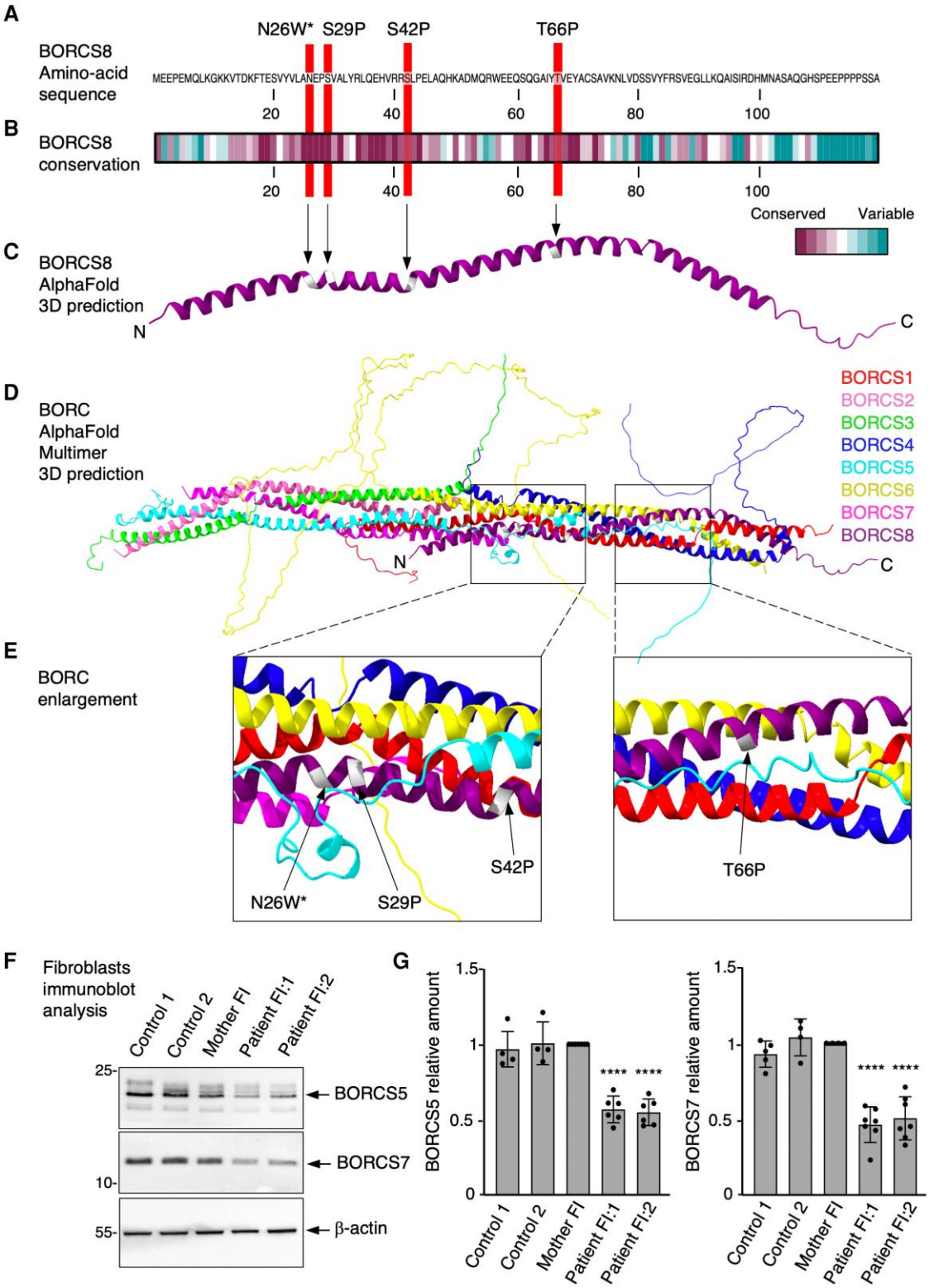

Figure 3 Characteristics of wild-type and variant *BORCS8* alleles. (**A**) Amino acid sequence of wild-type BORCS8 indicating the positions of the variants. (**B**) Amino acid conservation of BORCS8 from different species calculated on the ConSeq server[27] using default search values. (**C**) Structure of BORCS8 extracted from the whole BORC complex predicted by AlphaFold Multimer. (**D**) Structure of the BORC complex predicted by AlphaFold Multimer. (**E**) Close-up view of the positions of the variants. (**F**) Skin fibroblast cultures from two unrelated controls [a healthy individual (Control 1, 85E0344) and an SPG50 patient (Control 2, 87RD39)],[18,19] the unaffected Family FI mother and her affected children were analysed by SDS-PAGE and immunoblotting for the endogenous BORCS5 and BORCS7 subunits of BORC. β-Actin was used as loading control. The positions of molecular mass markers (in kDa) are indicated on the *left*. (**G**) Quantification of endogenous BORCS5 and BORCS7 levels from at least four independent experiments such as that shown in **F**. Values are the mean ± standard deviation (SD) from the number of data-points shown on the figure. Statistical significance was calculated by one-way ANOVA followed by multiple comparisons using Dunnett's test. ****$P < 0.0001$.

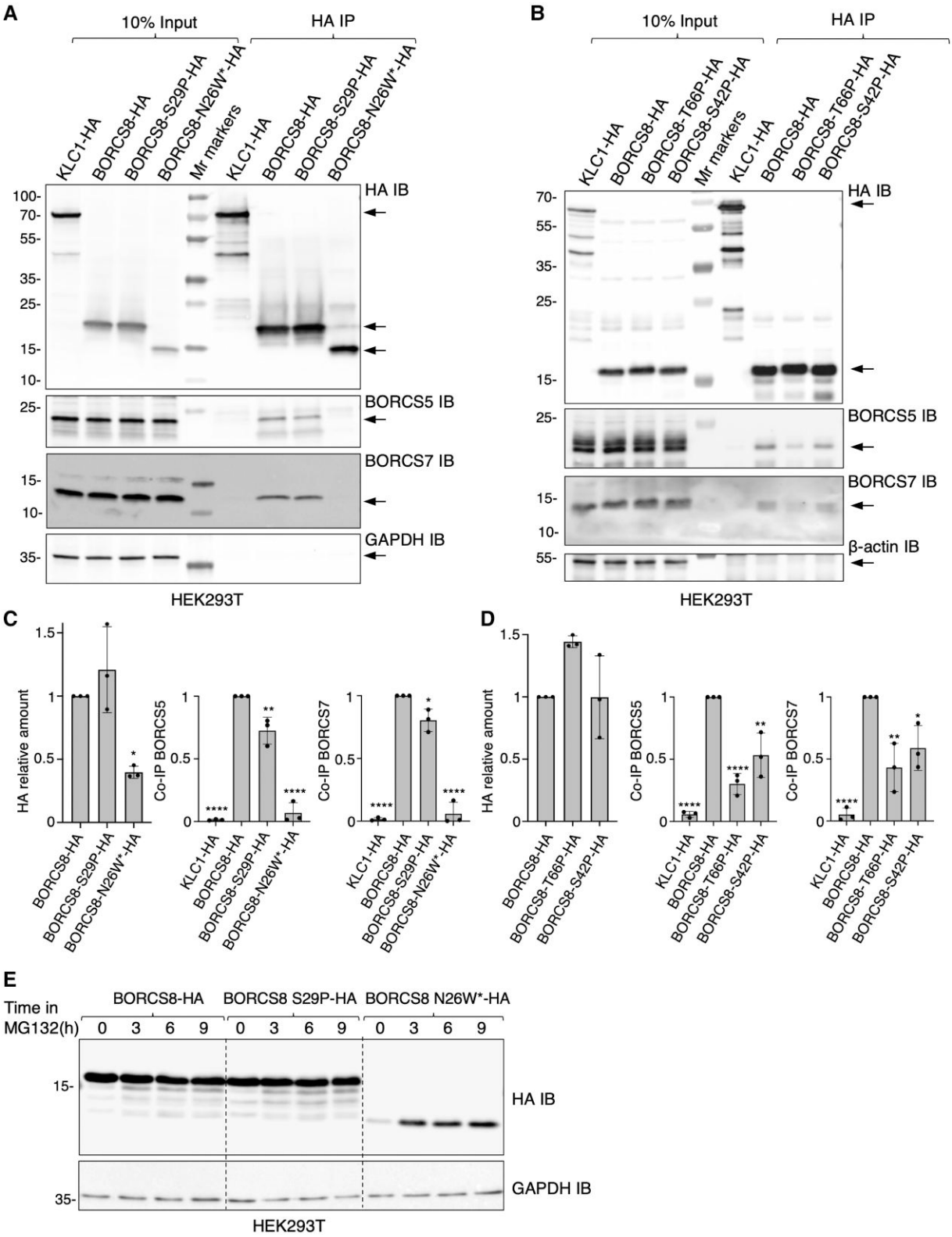

Figure 4 BORCS8 patient variants reduce the levels and/or assembly of BORC subunits. (**A** and **B**) HEK293T cells were transfected with plasmids encoding the indicated HA-tagged constructs and subjected to immunoprecipitation with antibody to the HA epitope. Cell extracts (10%) and immunoprecipitates (HA IP) were analysed by SDS-PAGE and immunoblotting (IB) for the HA epitope, endogenous BORCS5 and BORCS7, GAPDH (control) or β-actin (control). KLC1-HA was used as a non-specific immunoprecipitation control. The positions of molecular mass markers (in kDa) are indicated on the *left*. Arrows indicate the positions of the specific proteins. (**C** and **D**) Quantification from three independent experiments such as those shown in **A** and **B**. Values are the mean ± standard deviation (SD). Statistical significance was calculated by one-way ANOVA followed by multiple comparisons using Dunnett's test. $^{*}P < 0.05$; $^{**}P < 0.01$; $^{****}P < 0.0001$. (**E**) HEK293T cells transfected with HA-tagged BORCS8 constructs were treated with 40 μM of the proteasomal inhibitor MG132 for the indicated times, lysed and immunoblotted for the HA epitope and GAPDH (loading control). The positions of molecular mass markers (in kDa) are indicated on the *left*.

Immunoprecipitation from extracts of transfected HEK293T cells expressing BORCS8-HA constructs with antibody to the HA epitope, followed by immunoblotting for endogenous BORCS5 and BORCS7, showed that co-immunoprecipitation of these subunits was reduced to 30%–80% for the S29P, T66P and S42P mutants, and to ~5% for the N26W* mutant (Fig. 4A–D, HA IP lanes). The N26W* co-immunoprecipitation was indistinguishable from that obtained with the irrelevant KLC1-HA control (Fig. 4A and C), indicating that it was non-specific. From these experiments, we concluded that, despite being expressed at similar levels than wild-type BORCS8, the S29P, T66P and S42P mutants were partially impaired in their ability to assemble with other subunits of BORC. The N26W* mutant, on the other hand, was not only expressed at lower levels but was also completely incapable of assembling with other BORC subunits. The reduced assembly of the BORCS8 mutant proteins into the complex likely results in partial degradation of the other subunits, accounting for the reduced levels of both BORCS5 and BORCS7 in the patients' fibroblasts (Fig. 3F and G). These findings are in line with previous studies showing a requirement of all subunits for stable assembly of BORC.[9,28]

Decreased lysosome-dispersal activity of BORCS8 mutants

To investigate the functional properties of the patients' *BORCS8* variants, we performed rescue experiments with BORCS8-KO HeLa cells (Fig. 5A). Extracts from wild-type and BORCS8-KO HeLa cells showed reduced amounts of endogenous BORCS5 and BORCS7 proteins (Fig. 5B and C), but not of the corresponding mRNAs (Supplementary Fig. 4D). This confirmed that BORCS5 and BORCS7 were destabilized in the absence of BORCS8, and that all the subunits are necessary for assembly of a stable BORC.[9,28] Cycloheximide chase experiments showed increased turnover of BORCS5 and BORC7 in BORCS8-KO relative to wild-type HeLa cells (Supplementary Fig. 5A and B), demonstrating that the reduced levels of BORCS5 and BORCS7 in the absence of BORCS8 were due to enhanced degradation. As shown above for HEK293T cells (Fig. 4A–D), transfection of BORCS8-KO cells with plasmids encoding HA-tagged wild-type and mutant BORCS8 constructs showed that the wild-type, S29P, T66P and S42P proteins were expressed at similar levels, whereas the N26W* protein was expressed at lower levels (Fig. 5D).

Next, we examined the effect of expressing wild-type and mutant BORCS8 proteins on the distribution of lysosomes labelled for the endogenous lysosomal membrane protein LAMP1 in BORCS8-KO HeLa cells. In agreement with previous findings,[1,8] BORCS8 KO caused clustering of lysosomes in the juxtanuclear area of the cells and their depletion from the peripheral cytoplasm (Fig. 5E, G and H). Expression of wild-type BORCS8 restored the normal distribution of lysosomes (Fig. 5F–H). In contrast, expression of the BORCS8 mutants resulted in partial (S29P, T66P) or no rescue (N26W*, S42P) (Fig. 5F–H). These observations demonstrated that the patients' BORCS8 variants have reduced ability to distribute lysosomes toward the peripheral cytoplasm.

BORCS8 KO has also been shown to increase the levels of the autophagy protein LC3B, due to inhibition of lysosome-autophagosome fusion[23] (Supplementary Fig. 6A and C). We observed that re-expression of wild-type, S29P or T66P BORCS8 decreased the number of LC3B puncta in BORCS8-KO HeLa cells, whereas re-expression of N26W* and S42P BORCS8 did not (Supplementary Fig. 6B and C). From these experiments, we concluded that at least some of the BORCS8 mutants compromise the ability of lysosomes to fuse with autophagosomes. Differences in the activity of the S29P in T66P mutants in lysosome dispersal (Fig. 5) and LC3B reduction (Supplementary Fig. 6) may be due to the different sensitivity of each assay.

Neurodevelopmental defects in *borcs8*-KO zebrafish

A role for BORCS8 in neurodevelopment had not been demonstrated prior to this work. To assess this role in a vertebrate model, we examined the effect of knocking out *borcs8* in zebrafish. The zebrafish genome encodes a single *borcs8* orthologue that shares 67% nucleotide and 76% amino acid identity with human *BORCS8*/BORCS8. We generated a *borcs8* F0 KO model using CRISPR-Cas9.[30] To this end, we used three sets of Cas9-gRNA ribonucleoproteins (RNPs) to target *borcs8* (Supplementary Fig. 7A), thereby generating a biallelic zygotic KO directly in the injected embryos (F0 generation). Using a high-resolution melting assay,[31] we found that RNPs were very efficient in creating indels in injected embryos (Supplementary Fig. 7B). Sequencing of injected embryos revealed mutations at the targeted loci, with a high percentage of indels leading to premature stop codons (Supplementary Fig. 7C and D).

We found that at 3 days post-fertilization (3 dpf) *borcs8* F0 KO larvae exhibited a smaller body size (intermediate phenotype), with some of the larvae exhibiting a slight curvature of the body axis (strong phenotype) (Fig. 6A–C), as compared to wild-type controls. Injections of Cas9 protein alone as a control showed no morphological defects compared to wild-type larvae (Fig. 6A–C). Additionally, the *borcs8* F0 KO 3 dpf fish displayed a smaller head (Fig. 6D) and eye size (Fig. 6E) compared to wild-type controls and Cas9-expressing control fish. These morphological defects persisted at 5 dpf (Supplementary Fig. 8A–C). We further examined these fish at the histological level on transverse brain sections at 3 dpf (Supplementary Fig. 7E) and 5 dpf (Fig. 6F and G). Haematoxylin and eosin staining revealed significant structural differences and smaller brain size in 5 dpf brains from *borcs8* F0 KO relative to wild-type larvae (Fig. 6F and G). These differences were not evident at 3 dpf (Supplementary Fig. 7E), suggesting that structural brain abnormalities in *borcs8* F0 KO fish are progressive.

Normalization of head and eye areas to body length at 3 dpf revealed no differences in both ratios in *borcs8* F0 KO larvae compared to wild-type controls (Supplementary Fig. 8D and E). Similarly, no differences were observed in normalized head and brain areas to body length at 5 dpf, but the eye area:body length ratio was significantly reduced in *borcs8* F0 KO larvae (Supplementary Fig. 8F–H). Taken together, these data suggest a global developmental delay in *borcs8*-KO zebrafish, consistent with clinical findings in the children bearing mutations in *BORCS8*. To test the specify of the morphological phenotypes in *borcs8* KO fish, mRNA encoding human *BORCS8* (Rescue) was injected along with RNPs, resulting in significant rescue of the head, eye and brain areas, and the body length defects (Fig. 6C–E and G).

Given the clinical findings of hypotonia and limb spasticity in patients bearing *BORCS8* mutations, we assessed neuromuscular morphology and locomotion in *borcs8* F0 KO larvae. The areas of dorsal and ventral myotomes of 3 dpf *borcs8* F0 KO larvae were significantly reduced (Fig. 6H and I). Additionally, the myosepta of *borcs8* F0 KO larvae were markedly narrower than in control larvae (Fig. 6J). Along with these muscle phenotypes, we found that the motor neurons, which innervate the myotomes, have shorter and less branched axons (Fig. 7A and B). The motor axonal defects in *borcs8* F0 KO zebrafish

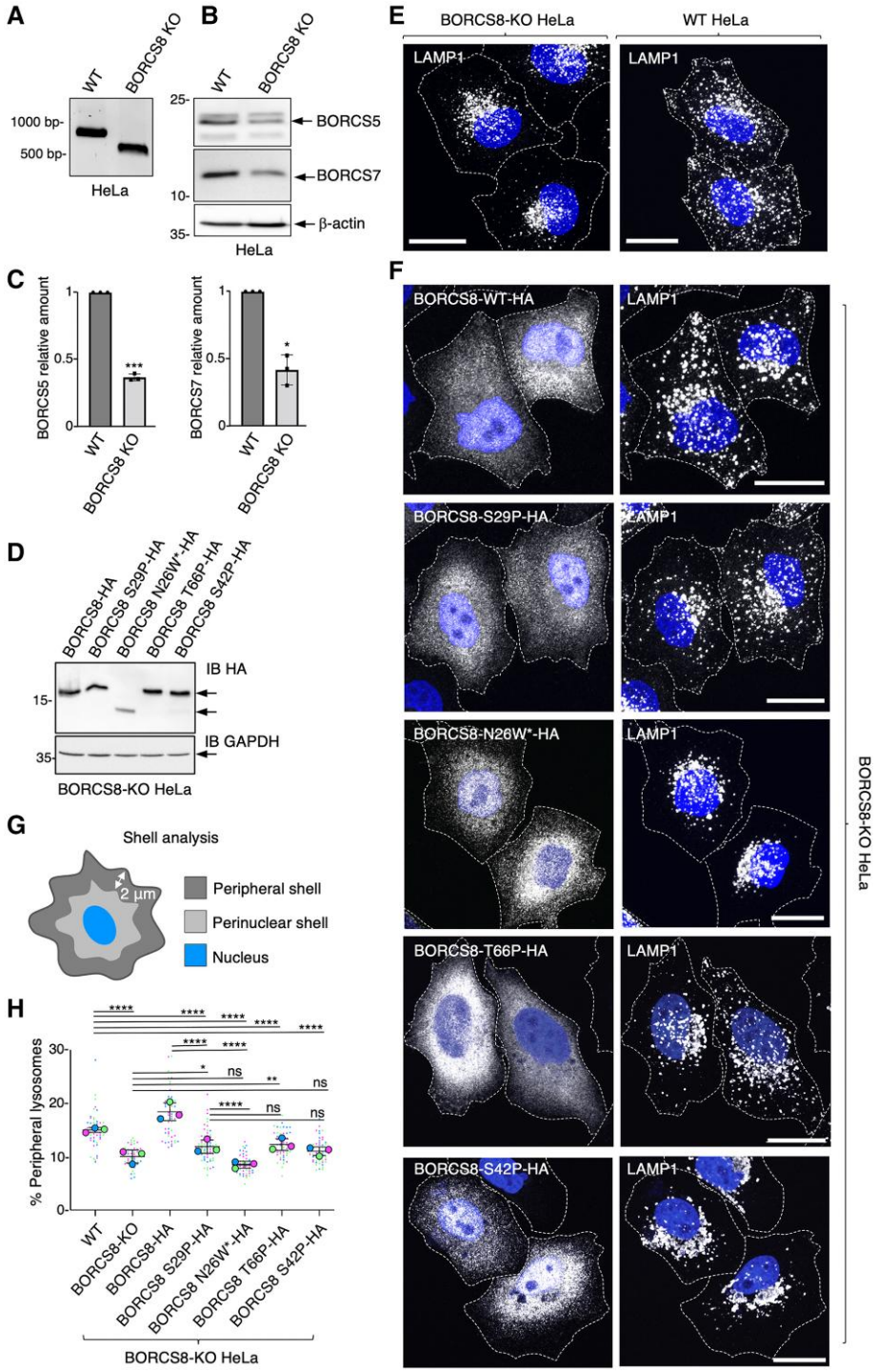

Figure 5 BORCS8 patient variants impair the lysosome-dispersal function of BORC. (**A**) Agarose gel electrophoresis and GelRed® staining of genomic *BORCS8* PCR products yields 745-bp fragment for wild-type (WT) and 513-bp fragment for BORCS8-KO HeLa cells. (**B**) SDS-PAGE and immunoblot analysis of wild-type and BORCS8-KO HeLa cells using antibodies to endogenous BORCS5 and BORCS7. β-Actin was used as a control. The positions of molecular mass markers (in kDa) are indicated on the *left*. (**C**) Quantification of BORCS5 and BORCS7 levels from three independent experiments such as that shown in **B**. Values are the mean ± standard deviation (SD). Statistical significance was calculated by Student's *t*-test. $^{*}P < 0.05$; $^{***}P < 0.001$. (**D**) BORCS8-KO HeLa cells were transiently transfected with the indicated HA-tagged BORCS8 constructs and cell extracts were immunoblotted (IB) for the HA epitope and GAPDH (loading control). The positions of molecular mass markers (in kDa) are indicated on the *left*. The positions of specific proteins are indicated by arrows. (**E**) Wild-type and BORCS8-KO HeLa cells were fixed, permeabilized and immunostained for the endogenous lysosomal protein LAMP1. Nuclei were labelled with DAPI (blue). Cell edges were outlined by staining of actin with fluorescent phalloidin (not shown) and indicated by dashed lines. Scale bars = 20 μm. (**F**) BORCS8-KO cells were transiently transfected with the indicated HA-tagged constructs and immunostained for the HA epitope and endogenous LAMP1 as described for **E**. (**G**) Schematic representation of shell analysis.[26] (**H**) Quantification by shell analysis of peripheral LAMP1 signal in HeLa cells from three experiments such as those shown in **E** and **F**. Data are presented as SuperPlots[29] showing the individual data-points, the mean from each experiment, and the mean ± SD of the means. Statistical significance was calculated by one-way ANOVA followed by multiple comparisons using Tukey's test. $^{*}P < 0.05$; $^{**}P < 0.01$; $^{****}P < 0.0001$; ns = not significant.

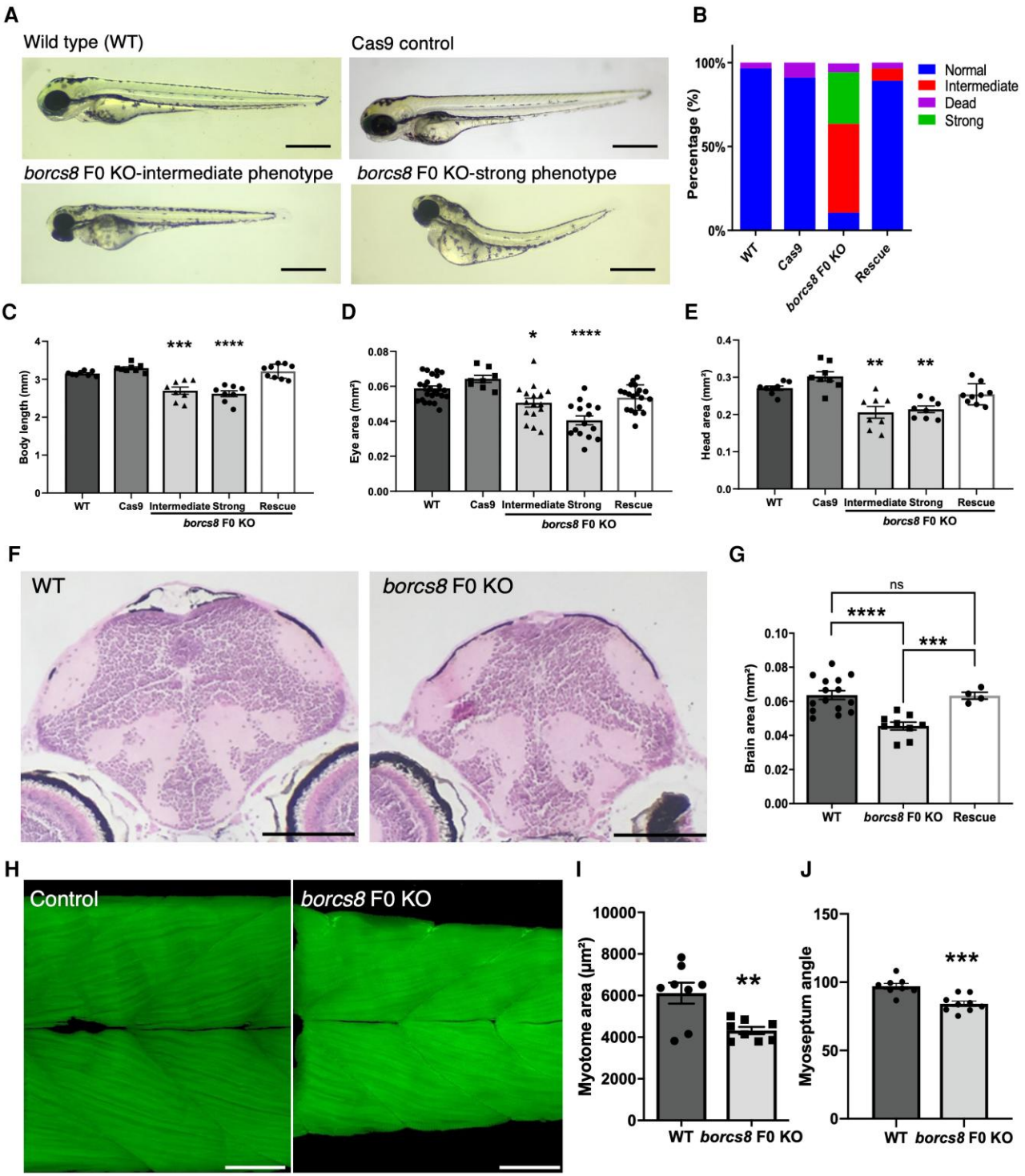

Figure 6 Zebrafish *borcs8* F0 knockout larvae exhibit developmental defects. (**A**) Morphology of zebrafish wild-type (WT), Cas9 control and *borcs8* F0 knockout (KO) larvae at 3 days post-fertilization (dpf). Scale bars = 1 mm. (**B**) Frequency of phenotypes observed for wild-type, Cas9 control, *borcs8* F0 KO and human *BORCS8* mRNA rescue (Rescue) larvae ($N = 4$, $n = 32–72$). (**C–E**) Body length (**C**), head size (**D**) and eye size (**E**) of wild-type, Cas9 control, *borcs8* F0 KO and Rescue larvae at 3 dpf ($N = 3$, $n = 8–9$ for head size and body length, $n = 16–18$ for eye size). (**F**) Haematoxylin and eosin staining of paraffin-embedded brain sections from the midbrain of 5 dpf wild-type and *borcs8* F0 KO larvae. Scale bar = 100 µm. (**G**) Quantification of brain size of *borcs8* F0 KO larvae ($N = 9$) relative to wild-type ($N = 15$) and Rescue ($N = 4$) at 5 dpf. (**H**) Phalloidin staining of muscles in *borcs8* F0 KO and wild-type larvae at 3 dpf. (**I** and **J**) Comparisons of dorsal or ventral myotome area (**I**) and myoseptum angle (**J**) between wild-type ($N = 3$, $n = 8$) and *borcs8* F0 KO larvae ($N = 3$, $n = 8–9$). All data are represented as the mean ± standard error of the mean (SEM). Statistical significance was calculated by one-way ANOVA followed by Tukey's multiple comparisons tests, or Student's *t*-test. $^{*}P < 0.05$; $^{**}P < 0.01$; $^{***}P < 0.001$; $^{****}P < 0.0001$. N = replicates; n = sample size; ns = not significant.

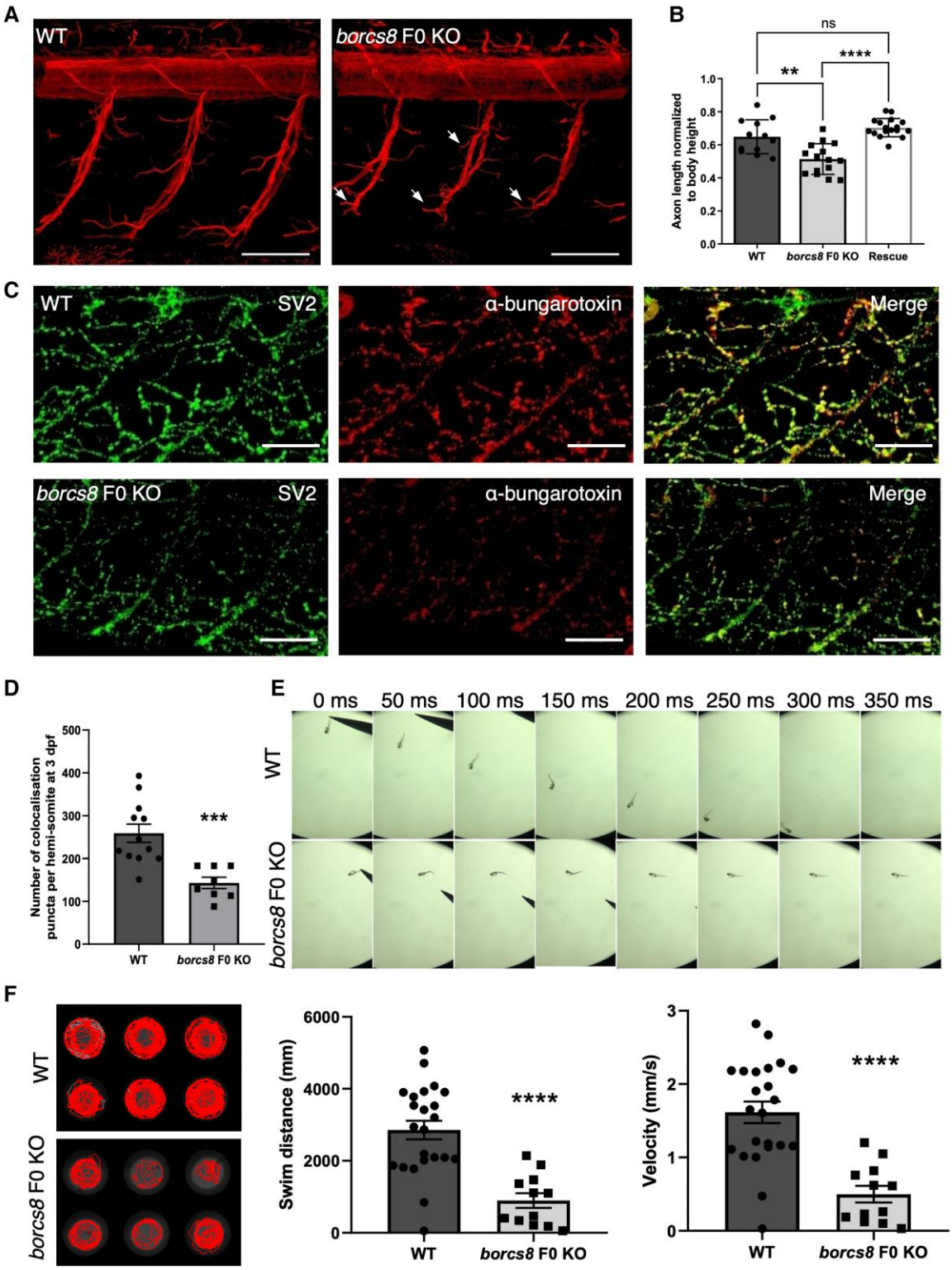

Figure 7 Neuromuscular defects and impaired motility in *borcs8* F0 knockout zebrafish larvae. (**A**) Primary motor axons in wild-type (WT) and *borcs8* F0 knockout (KO) larvae at 3 days post-fertilization (dpf). Scale bars = 50 μm. Defects in axon branching are indicated by white arrows. (**B**) Quantification shows marked reduction in the axon length of motor neurons in *borcs8* F0 KO ($N = 3$, $n = 15$) compared to WT ($N = 3$, $n = 12$) and Rescue larvae ($N = 3$, $n = 18$). (**C**) Co-immunostaining of zebrafish neuromuscular junctions (NMJs) with presynaptic (SV2; green) and postsynaptic (α-bungarotoxin; red) markers in 3 dpf zebrafish. Scale bars = 50 μm. (**D**) Quantification of co-localizing presynaptic and postsynaptic markers per hemisomite, normalized to the number of presynaptic puncta, showed a significant reduction in the number of puncta in *borcs8* F0 KO larvae ($N = 3$–4, $n = 8$–12). (**E**) Representative snapshots of touch escape responses ($N = 6$) over 350 ms. Zebrafish *borcs8* F0 KO larvae have very little to no escape response at 2 dpf. (**F**) Representative swimming tracks of wild-type control and *borcs8* F0 KO fish at 5 dpf. The *borcs8* F0 KO larvae ($N = 3$, $n = 32$) displayed impaired swim distance and velocity compared to controls ($N = 3$, $n = 24$). All data are represented as the mean ± standard error of the mean (SEM). Statistical significance was calculated by Student's *t*-test, or one-way ANOVA followed by Tukey's multiple comparisons tests. $^{**}P < 0.01$; $^{***}P < 0.001$; $^{****}P < 0.0001$. N = replicates; n = sample size; ns = not significant.

were significantly rescued upon expression of the human *BORCS8* mRNA (Fig. 7B). We next examined NMJ integrity by performing double immunohistochemistry using specific presynaptic (SV2) and postsynaptic (α-bungarotoxin) markers. We observed a drastic alteration in NMJ morphology with reduced presynaptic and postsynaptic staining in 3 dpf (Fig. 7C) and 5 dpf (Supplementary Fig. 9A) *borcs8* F0 KO larvae compared to wild-type controls, and a reduction in the number of co-localizing presynaptic and postsynaptic puncta in *borcs8* F0 KO larvae (Fig. 7D and Supplementary Fig. 9B). This decrease in synaptic puncta at NMJs in *borcs8* F0 KO fish was accompanied by a significant reduction in AChE activity (Supplementary Fig. 9C). Further analysis revealed no change in co-localization of presynaptic and postsynaptic puncta in *borcs8* F0 KO at early embryonic developmental stages (2 dpf; Supplementary Fig. 9D and E). However, 2 dpf *borcs8* F0 KO larvae displayed impaired movement after touch (i.e. touch-evoked escape response) (Fig. 7E), and 5 dpf larvae decreased locomotor activity (i.e. free swimming), as compared to controls (Fig. 7F). No significant changes in free-swimming activity between *borcs8* F0 KO fish and wild-type controls were observed at early developmental stages (2 and 3 dpf; Supplementary Fig. 9F and G). These findings thus indicated that *borcs8* F0 KO larvae had neuromuscular defects with a strong impact on motor function. Moreover, our data suggest that the defects in NMJ morphology and locomotor activity were progressive with larval age, consistent with the neurodegenerative findings in patients bearing *BORCS8* mutations.

Discussion

Here we report on five children from three unrelated families with biallelic variants in *BORCS8*. These children present with global developmental delay, severe-to-profound intellectual disability, facial dysmorphism, variable neurological features including seizures, spasticity, stereotypies, cortical visual impairment and consistent neuroradiological findings. The latter include cerebral and cerebellar atrophy, white matter hypomyelination, hypoplasia of the pons, thin corpus callosum, small thalami and optic atrophy. In addition, focal white matter signal alterations with an 'ears of the lynx' sign were noted in two subjects, and T_2 hypointensity of globus pallidi was evident in another patient. Many of these features were apparent on initial MRI scans at the age of 1–3 years, with the rest becoming noticeable on follow-up scans several years later. In line with these findings, biallelic KO of *borcs8* in zebrafish leads to neurodevelopmental defects and loss of motility. These findings demonstrate that BORCS8 is critical for the development and function of the CNS in vertebrates.

The neuroimaging findings in the BORCS8-deficient patients overlap with those of other congenital neurological disorders and, in combination, could help with the diagnosis of this condition. Hypomyelination is a key feature of a large number of disorders, many of which present with developmental disability (DD), intellectual disability (ID) and/or facial dysmorphism.[32] Among these disorders are Pelizaeus-Merzbacher disease, Pelizaeus-Merzbacher-like disease, 4H syndrome, Salla disease, hypomyelination and congenital cataract, and 18q deletion syndrome.[32] Of note, hypomyelination associated with neurodegenerative features is also common in infantile-onset lysosomal neuronal storage disorders, such as infantile GM1 and GM2 gangliosidosis, fucosidosis and neuronal ceroid lipofuscinoses, in which myelination is perturbed due to axonal dysfunction and degeneration starting before myelination has reached completion.[33]

Small thalami are a feature of postnatal progressive microcephaly with seizures and brain atrophy caused by biallelic variants in *MED17*,[34] and neurodevelopmental disorder with seizures and brain atrophy caused by biallelic variants in *EXOC7*.[35] Thin corpus callosum with 'ear of the lynx sign' can be seen in hereditary spastic paraplegia due to biallelic *SPG11* and *SPG15* variants, both characterized by lysosomal dysfunction.[36] Neurodevelopmental impairments with T_2 hypointensity of the globus pallidi in children suggests connections to a form of neurodegeneration with brain iron accumulation (NBIA).[37,38] NBIA is now a fairly large group of disorders, but childhood-onset NBIA with MRI features overlapping with those seen in children with biallelic *BORCS8* variants (i.e. globus pallidi T_2 hypointensity plus white matter changes) include infantile neuroaxonal dystrophy (NBIA2A), fatty acid hydroxylase-associate neurodegeneration (FAHN; also called hereditary spastic paraplegia type 35), Kufor-Rakeb syndrome and Woodhouse-Sakati syndrome.[37,38] However, when these MRI features are seen in association with progressive cerebral and cerebellar atrophy, optic atrophy and hypoplasia of the pons in a child with DD/ID, abnormal neurology and facial dysmorphism, BORCS8-related disorder should be considered a likely diagnosis.

The clinical features of the patients with *BORCS8* variants described here are also like those of a previously reported patient with a homozygous splice variant of *BORCS5* (c.203-1G>T).[17] The exact nature of the transcript and the activity of the BORCS5 variant protein were not assessed in the previous study. Nevertheless, the similarities in clinical presentation suggest that the BORCS5 variant protein may likewise be defective in expression, assembly and/or function. Together, these findings begin to define a 'BORC-deficiency syndrome' caused by variants in any of the subunits of this complex, in the same way that an 'AP-4 deficiency syndrome' (a form of hereditary spastic paraplegia) is caused by variants in subunits of the AP-4 complex.[39,40]

The BORCS8 S29P, T66P and S42P substitutions are all predicted to be deleterious by bioinformatics tools. Their deleterious effects are likely due to destabilization of the long α-helix by the irregular geometry of the substitute Pro. The N26W* variant, on the other hand, results in deletion of most of the long α-helix and its partial replacement by an irrelevant sequence. This latter variant has little of the normal BORCS8 and is thus also expected to be deleterious. Indeed, analyses using a heterologous cell system show that all BORCS8 variants are functionally defective (Supplementary Table 4). In transfected HEK293T and HeLa cells, the S29P, T66P and S42P proteins are expressed at normal levels but display reduced assembly with BORCS5 and BORCS7. Furthermore, the N26W* protein is expressed at very low levels because of proteasomal degradation and does not assemble at all with BORCS5 and BORCS7. KO or mutations in BORC subunit genes were previously shown to cause destabilization and degradation of other subunits of the complex.[1,9,11,28] This phenomenon may account for the reduced levels of BORCS5 and BORCS7 in skin fibroblasts of the Family FI affected siblings relative to those of the mother.

The variant BORCS8 proteins displayed not only expression and/or assembly defects but also decreased ability to rescue lysosome dispersal in BORCS8-KO cells. BORC is part of an adaptor system that couples lysosomes to kinesin-1 and -3 motors for anterograde transport along microtubule tracks.[1,8] Accordingly, we found that KO of BORCS8 impairs the distribution of lysosomes toward the peripheral cytoplasm, causing their clustering in the juxtanuclear area of the cell. Whereas re-expression of wild-type BORCS8 restored the normal distribution of lysosomes, all the variants displayed reduced activity in this assay. We were unable to assess the

distribution of lysosomes in fibroblasts from the Family F1 siblings versus their mother because the spindly shape of the fibroblasts and proximity of lysosomes to the nucleus precluded accurate quantification of lysosome distribution. Taken together, the above findings demonstrated that the BORCS8 variants analysed in this study are likely pathogenic.

The severity of phenotypic defects in mice and humans with mutations in BORC-subunit genes emphasizes the critical importance of lysosome distribution for the maintenance of cellular homeostasis. This importance derives from the need to distribute not only the degradative activity of lysosomes, but also their non-degradative roles in signalling, adhesion and plasma membrane repair to all regions of the cell.[1,41] This ability is even more critical in neurons, where lysosomes are required for maintenance of axonal health. In our functional assay, we focused on the function of BORC in promoting anterograde lysosome transport. However, BORC also mediates ARL8-dependent recruitment of RUFY3, a regulator of lysosome coupling to the retrograde microtubule motor dynein-dynactin[42,43] and the HOPS complex, a regulator of endolysosomal/autophagosomal tethering and fusion.[23,44,45] Indeed, BORCS-KO HeLa cells exhibited accumulation of the autophagy protein LC3B, which was reversed by re-expression of wild-type but not N26W* or S42P BORCS8. It is thus likely that BORCS8-deficient patients also have endolysosomal/autophagosomal fusion defects that contribute to the pathogenesis of the disease.

Loss-of-function of *borcs8* in zebrafish resulted in neurodevelopmental defects including reduced muscle size, motor axon defects, NMJ anomalies and impaired motility, further supporting a role for borcs8 in the development and function of the CNS. Some of these defects were progressive, consistent with the presentation of the disease in humans. These findings are in line with those in previous studies of BORCS5 and BORCS7 mutant mice, which displayed a number of neurodevelopmental abnormalities.[9,11] For instance, BORCS7 Q87X/Q87X-mutant mice exhibited motor axonal atrophy and impaired motor function.[11] One difference with the *borcs8* F0 KO zebrafish is that BORCS5-KO mouse embryos did not display defects in the diaphragm NMJs, although the innervating phrenic nerve was severely dystrophic.[9] This differential effect on NMJs could be due to differences in species, developmental stage, specific NMJs or BORC subunits mutated. It is noteworthy that BORCS5-KO and BORCS7-KO mice die neonatally.[9,11] It is thus likely that BORCS8 KO would also be lethal in mice and humans, and that the partial activity of some of the variants keeps the patients alive, albeit with severe CNS problems.

In summary, our results identify *BORCS8* as a novel neurogenetic disease gene, and BORC-dependent lysosome dynamics as a critical process in human CNS development and function.

Data availability

The data that support the findings of this study are available from the corresponding author, upon reasonable request.

Acknowledgements

We thank the patients and their parents for their participation in this study. We also thank Carsten Bönnemann (NINDS, NIH) and Christopher Grunseich (NINDS, NIH) for helpful discussions. This work utilized the computational resources of the NIH HPC Biowulf cluster (http://hpc.nih.gov).

Funding

The study was funded by the generous gifts to Children's Mercy Research Institute and Genomic Answers for Kids program at Children's Mercy Kansas City, the Intramural Program of the Eunice Kennedy Shriver National Institute of Child Health and Human Development (NICHD) (project ZIA HD001607 to J.S.B.), Wellcome Trust, Medical Research Council, The MSA Trust, The National Institute for Health Research University College London Hospitals Biomedical Research Centre, Michael J. Fox Foundation (MJFF), BBSRC, The Fidelity Trust, Rosetrees Trust, Ataxia UK, Brain Research UK, Great Ormond Street Hospital Charity, Alzheimer's Research UK (ARUK) and CureDRPLA (to R.M.) and the Canadian Institutes of Health Research (CIHR, OGB-177940 to S.A.P.).

Competing interests

The authors report no competing interests.

Supplementary material

Supplementary material is available at *Brain* online.

References

1. Pu J, Schindler C, Jia R, Jarnik M, Backlund P, Bonifacino JS. BORC, a multisubunit complex that regulates lysosome positioning. *Dev Cell*. 2015;33:176-188.
2. Filipek PA, de Araujo MEG, Vogel GF, et al. LAMTOR/ragulator is a negative regulator of Arl8b- and BORC-dependent late endosomal positioning. *J Cell Biol*. 2017;216:4199-4215.
3. Pu J, Keren-Kaplan T, Bonifacino JS. A ragulator-BORC interaction controls lysosome positioning in response to amino acid availability. *J Cell Biol*. 2017;216:4183-4197.
4. Schweitzer LD, Comb WC, Bar-Peled L, Sabatini DM. Disruption of the Rag-ragulator complex by c17orf59 inhibits mTORC1. *Cell Rep*. 2015;12:1445-1455.
5. Hofmann I, Munro S. An N-terminally acetylated Arf-like GTPase is localised to lysosomes and affects their motility. *J Cell Sci*. 2006;119:1494-1503.
6. Rosa-Ferreira C, Munro S. Arl8 and SKIP act together to link lysosomes to kinesin-1. *Dev Cell*. 2011;21:1171-1178.
7. Niwa S, Lipton DM, Morikawa M, et al. Autoinhibition of a neuronal kinesin UNC-104/KIF1A regulates the size and density of synapses. *Cell Rep*. 2016;16:2129-2141.
8. Guardia CM, Farías GG, Jia R, Pu J, Bonifacino JS. BORC functions upstream of kinesins 1 and 3 to coordinate regional movement of lysosomes along different microtubule tracks. *Cell Rep*. 2016;17:1950-1961.
9. De Pace R, Britt DJ, Mercurio J, et al. Synaptic vesicle precursors and lysosomes are transported by different mechanisms in the axon of mammalian neurons. *Cell Rep*. 2020;31:107775.
10. Farías GG, Guardia CM, De Pace R, Britt DJ, Bonifacino JS. BORC/kinesin-1 ensemble drives polarized transport of lysosomes into the axon. *Proc Natl Acad Sci U S A*. 2017;114:E2955-E2964.
11. Snouwaert JN, Church RJ, Jania L, et al. A mutation in the Borcs7 subunit of the lysosome regulatory BORC complex results in motor deficits and dystrophic axonopathy in mice. *Cell Rep*. 2018;24:1254-1265.

12. Schiefermeier N, Scheffler JM, de Araujo ME, et al. The late endosomal p14-MP1 (LAMTOR2/3) complex regulates focal adhesion dynamics during cell migration. *J Cell Biol*. 2014;205:525-540.
13. Dykes SS, Gray AL, Coleman DT, et al. The Arf-like GTPase Arl8b is essential for three-dimensional invasive growth of prostate cancer in vitro and xenograft formation and growth in vivo. *Oncotarget*. 2016;7:31037-31052.
14. Michelet X, Tuli A, Gan H, et al. Lysosome-mediated plasma membrane repair is dependent on the small GTPase Arl8b and determines cell death type in Mycobacterium tuberculosis infection. *J Immunol*. 2018;200:3160-3169.
15. Jia R, Bonifacino JS. Lysosome positioning influences mTORC2 and AKT signaling. *Mol Cell*. 2019;75:26-38.e3.
16. Korolchuk VI, Saiki S, Lichtenberg M, et al. Lysosomal positioning coordinates cellular nutrient responses. *Nat Cell Biol*. 2011;13:453-460.
17. Charng WL, Karaca E, Coban Akdemir Z, et al. Exome sequencing in mostly consanguineous Arab families with neurologic disease provides a high potential molecular diagnosis rate. *BMC Med Genomics*. 2016;9:42.
18. Verkerk AJ, Schot R, Dumee B, et al. Mutation in the AP4M1 gene provides a model for neuroaxonal injury in cerebral palsy. *Am J Hum Genet*. 2009;85:40-52.
19. De Pace R, Skirzewski M, Damme M, et al. Altered distribution of ATG9A and accumulation of axonal aggregates in neurons from a mouse model of AP-4 deficiency syndrome. *PLoS Genet*. 2018;14:e1007363.
20. Bertoli-Avella AM, Kandaswamy KK, Khan S, et al. Combining exome/genome sequencing with data repository analysis reveals novel gene-disease associations for a wide range of genetic disorders. *Genet Med*. 2021;23:1551-1568.
21. Cohen ASA, Farrow EG, Abdelmoity AT, et al. Genomic answers for children: Dynamic analyses of >1000 pediatric rare disease genomes. *Genet Med*. 2022;24:1336-1348.
22. Dafsari HS, Pemberton JG, Ferrer EA, et al. PI4K2A deficiency causes innate error in intracellular trafficking with developmental and epileptic-dyskinetic encephalopathy. *Ann Clin Transl Neurol*. 2022;9:1345-1358.
23. Jia R, Guardia CM, Pu J, Chen Y, Bonifacino JS. BORC coordinates encounter and fusion of lysosomes with autophagosomes. *Autophagy*. 2017;13:1648-1663.
24. Westerfield M. *The zebrafish book: a guide for the laboratory use of zebrafish*. 4th ed. Univ. of Oregon Press; 2000.
25. Kimmel CB, Ballard WW, Kimmel SR, Ullmann B, Schilling TF. Stages of embryonic development of the zebrafish. *Dev Dyn*. 1995;203:253-310.
26. Williamson CD, Guardia CM, De Pace R, Bonifacino JS, Saric A. Measurement of lysosome positioning by shell analysis and line scan. *Methods Mol Biol*. 2022;2473:285-306.
27. Berezin C, Glaser F, Rosenberg J, et al. ConSeq: The identification of functionally and structurally important residues in protein sequences. *Bioinformatics*. 2004;20:1322-1324.
28. Yordanov TE, Hipolito VEB, Liebscher G, et al. Biogenesis of lysosome-related organelles complex-1 (BORC) regulates late endosomal/lysosomal size through PIKfyve-dependent phosphatidylinositol-3,5-bisphosphate. *Traffic*. 2019;20:674-696.
29. Lord SJ, Velle KB, Mullins RD, Fritz-Laylin LK. SuperPlots: Communicating reproducibility and variability in cell biology. *J Cell Biol*. 2020;219:e202001064.
30. Kroll F, Powell GT, Ghosh M, et al. A simple and effective F0 knockout method for rapid screening of behaviour and other complex phenotypes. *Elife*. 2021;10:e59683.
31. Samarut É, Lissouba A, Drapeau P. A simplified method for identifying early CRISPR-induced indels in zebrafish embryos using High Resolution Melting analysis. *BMC Genomics*. 2016;17:547.
32. Steenweg ME, Vanderver A, Blaser S, et al. Magnetic resonance imaging pattern recognition in hypomyelinating disorders. *Brain*. 2010;133:2971-2982.
33. van der Knaap MS, Bugiani M. Leukodystrophies: A proposed classification system based on pathological changes and pathogenetic mechanisms. *Acta Neuropathol*. 2017;134:351-382.
34. Kaufmann R, Straussberg R, Mandel H, et al. Infantile cerebral and cerebellar atrophy is associated with a mutation in the MED17 subunit of the transcription preinitiation mediator complex. *Am J Hum Genet*. 2010;87:667-670.
35. Coulter ME, Musaev D, DeGennaro EM, et al. Regulation of human cerebral cortical development by EXOC7 and EXOC8, components of the exocyst complex, and roles in neural progenitor cell proliferation and survival. *Genet Med*. 2020;22:1040-1050.
36. Edmison D, Wang L, Gowrishankar S. Lysosome function and dysfunction in hereditary spastic paraplegias. *Brain Sci*. 2021;11:152.
37. Lee JH, Yun JY, Gregory A, Hogarth P, Hayflick SJ. Brain MRI pattern recognition in neurodegeneration with brain iron accumulation. *Front Neurol*. 2020;11:1024.
38. Lehéricy S, Roze E, Goizet C, Mochel F. MRI of neurodegeneration with brain iron accumulation. *Curr Opin Neurol*. 2020;33:462-473.
39. Ebrahimi-Fakhari D, Teinert J, Behne R, et al. Defining the clinical, molecular and imaging spectrum of adaptor protein complex 4-associated hereditary spastic paraplegia. *Brain*. 2020;143:2929-2944.
40. Mattera R, De Pace R, Bonifacino JS. The role of AP-4 in cargo export from the trans-Golgi network and hereditary spastic paraplegia. *Biochem Soc Trans*. 2020;48:1877-1888.
41. Ballabio A, Bonifacino JS. Lysosomes as dynamic regulators of cell and organismal homeostasis. *Nat Rev Mol Cell Biol*. 2020;21:101-118.
42. Kumar G, Chawla P, Dhiman N, et al. RUFY3 links Arl8b and JIP4-dynein complex to regulate lysosome size and positioning. *Nat Commun*. 2022;13:1540.
43. Keren-Kaplan T, Sarić A, Ghosh S, et al. RUFY3 and RUFY4 are ARL8 effectors that promote coupling of endolysosomes to dynein-dynactin. *Nat Commun*. 2022;13:1506.
44. Garg S, Sharma M, Ung C, et al. Lysosomal trafficking, antigen presentation, and microbial killing are controlled by the Arf-like GTPase Arl8b. *Immunity*. 2011;35:182-193.
45. Khatter D, Sindhwani A, Sharma M. Arf-like GTPase Arl8: Moving from the periphery to the center of lysosomal biology. *Cell Logist*. 2015;5:e1086501.